ANALYSIS OF DATA FROM VIKING RPA's

NASA GRANT NSG-7599
UTD ACCOUNT E1264

FINAL TECHNICAL REPORT

1 March 1979 through 31 December 1980

W. B. Hanson
Principal Investigator

(NASA-CR-164192) ANALYSIS OF DATA FROM VIKING RPA'S Final Technical Report, 1 Mar. 1979 - 31 Dec. 1980 (Texas Univ. at Dallas.) 30 p HC A03/MF A01 CSCL 03B

N81-22998

Unclas
G3/91 42101

CENTER FOR SPACE SCIENCES
THE UNIVERSITY OF TEXAS AT DALLAS
P.O. BOX 688
RICHARDSON, TEXAS 75080

MAY 1981

ABSTRACT

In addition to the published RPA data that were taken in the Martian ionosphere, there exist many Viking RPA measurements of low energy (< 75 ev) electron fluxes out to 16,000 km above the Mars surface. Both energy spectra and periods of continuous monitoring of the total flux above 15 ev are available. The mean electron current at energies > 15 ev increases monotonically by nearly two orders of magnitude from about 9000 km down to 700 km, but no clear signature of the bow shock is seen. The total wave power in the two-second measurement intervals for this current does, however, show a broad peak near 1700 km altitude. These variations in the low energy electron fluxes can be related to whistler mode oscillations in the solar wind plasma. It is concluded that there may be a highly turbulent shock structure that would mask a clear signature of the bow shock in the time averaged data.

Introduction

On July 20, 1976 and September 31, 1976 the Viking landers descended through the near Mars environment down to the surface of Mars. The trajectories of the two spacecraft plotted as a function of altitude and solar zenith angle are shown in figure 1. While the spacecraft landed at nearly the same zenith angles, they followed quite different paths and landed about 6 hours apart in local time. The only plasma measuring device carried by the landers was a planar Retarding Potential Analyzer (RPA) that operated in both ion and electron modes.

The first successful in situ measurements of the Martian ionosphere were performed by these Viking RPA's. These low altitude data have been analyzed and the results have been published in the special Viking Issue of the Journal of Geophysical Research (Hanson et al., 1977). The sensible ionosphere was detected only as high as 350 km altitude, but data were received from the RPA from the time of the deorbit burn at 16,000 km altitude, some 160 minutes before entry. The high-altitude measurements from Lander 1 reflect mostly the currents that arise from low energy electrons in the ambient solar wind, in the shocked solar wind adjacent to Mars, and from shock precursor electrons. A large flux of electrons with a characteristic energy of $\sim$3 ev probably arose from photoemission off the spacecraft. It seems unlikely that Lander 2 obtained any data outside the bow shock. The data show definite evidence of the interaction of the solar wind with Mars. It is the purpose of this paper to describe these high altitude results and to discuss what they reveal about the nature of the Mars-solar wind interaction. Considerable interest in the preshocked solar wind near

earth has evolved in recent years, culminating in a workshop at JPL in April of 1980, which has been summarized by Tsurutani and Rodriguez (1980).

A brief description of the RPA instrumentation and its operational modes will be presented first. The nature of the raw data returned will also be described, followed by summary plots of different measured parameters versus time (altitude). Among these parameters are the energy spectra of the low energy electrons, as well as characteristics of the variability of the low energy electron fluxes. It is argued that these variations are related to whistler mode oscillations, and it is concluded that there may be a highly turbulent shock structure that could mask a clear signature of the bow shock in the time averaged data. Finally, a summary of the observations and their interpretation is given.

Instrumentation

A brief discussion of the sensor, the data format, and the nature of the data itself is given below. The geometry of the Viking RPA sensor head is shown in figure 2. The two entrance grids (G_1 and G_2) are grounded to the vehicle. The next two grids (G_3 and G_4) are the retarding (sweep) grids, to which a time-varying electric potential is applied. The suppressor grid (G_5) is held at different fixed potentials. G_6 and G_7 are shield grids that protect the collector from capacitively coupled electrical transients. The unusual rounded nature of the entrance aperture was invoked to prevent burn-through of the heat shield during entry.

A complete instrument operation cycle consists of four major frames, each of 4-second duration. The retarding grid is stepped through 3 different voltage ramps during a major frame. During the one-second energetic-electron-flux phase (Phase I), the retarding grid voltage moves from -75 V to 0 V in 100 equal voltage increments of 0.75 V, as shown in the top trace of figure 3.

During the thermal-electron-flux phase (Phase II), also one second long, the retarding grid voltage moves in 100 equal steps from -1.5 volts to 0 V. In Phase III, the two-second thermal-ion mode, the retarding grid goes from +15 V to 0 volts in 200 equal steps.

While the retarding-grid potential cycles as described above, the suppressor-grid potential changes as shown in the lower trace of figure 3. On alternate major frames, the suppressor grid is held either at +15 V or -4 V during Phase I. On every major frame, the suppressor grid is held at +15 V for Phase II and -15 V for Phase III. Thus we have two basically different major frames as distinguished by the suppressor grid behavior. Table 1 lists retarding grid potential, suppressor grid potential and electrometer sensitivity for the different major frames.

The RPA electrometer is a linear automatic-range-changing device with 8 sensitivity ranges differing successively by a factor of 4. At the beginning of each major frame the electrometer output is set to zero while the retarding grids are at -75 volts and the suppressor is at +15 volts. This procedure was adopted to avoid zero-drift in the electrometer during the long period while the instrument was idle, but means that the flux of electrons with energy greater than 75 ev could not be measured. On every fourth major frame, the electrometer is rezeroed on sensitivity range 5, rather than on range 1 (the most sensitive range). Therefore, a complete operation cycle consists of four major frames, as detailed in Table 1, where it can be seen that frames 1 and 3 are identical.

The RPA recorded data over the altitude range from approximately 16,000 km to 100 km for both landers, but the instruments operated intermittently over this range. They were on for 64 sec, then off for 325 sec

until 40 minutes before "entry" (which was arbitrarily defined to be 800,000 ft. altitude). During the final 45 minutes or so (below approximately 5000 km), operation was continuous.

Observations

Plots of four of the current vs. retarding potential characteristic curves (Phase I from major frame 2) recorded at different altitudes on Viking I are shown in figure 4. The places they were recorded are indicated by A, B, C, and D in figure 1.

Curve A is typical of the data recorded at large distances (large zenith angles). It has a large flux of low energy electrons with an e-folding energy of approximately 3 ev. This is a considerably smaller energy than the 10 to 20 ev that characterizes the solar wind electrons at 1 Au, and is also smaller by at least a factor of 2 than would be expected at Mars if the solar wind electrons are presumed to cool off as $R^{-2/7}$ (Hundhausen, 1970). It is quite likely that these currents arise from photoelectrons driven off the back side of the spacecraft by solar UV. The RPA sensor is mounted with its entrance grid flush to the aeroshell, which was never sunlit on its front face during the RPA operations. The entire aeroshell had a conducting surface to which the RPA sensor was grounded. Since the gyroradius of these electrons is large compared to spacecraft dimensions, the spacecraft would have to be charged positively to several volts potential with respect to the ambient plasma in order for the photoelectrons to have access to the RPA sensor. It does not seem unreasonable that this should be the case. This further implies that the ambient electrons impinging on the RPA should all have their energies increased by this potential difference before they strike the RPA sensors. Under certain idealized conditions it can be argued that if the spacecraft had a positive potential ψ then only photoelectrons with energy less than $e\psi$ would return to the spacecraft. Since all ambient electrons would have their energies at the

collector increased by $e\psi$ the spectrum could be divided cleanly into two regimes at the potential ψ. Above energy $e\psi$ all currents would be due to ambient electrons and all increases in current below this energy could be due to photoelectrons. In fact the low energy spectrum is remarkably constant in magnitude and shape above 2000 km altitude. There is usually a break in the slope near 6 volts, which could be interpreted as the spacecraft potential. At higher energies the curve is not a simple exponential, even when the imposed zero current at 75 volts is taken into account. There usually appear to be two additional characteristic energies, one that is approximately twice the photoelectron energy and the second is tens of ev. The intermediate energy current is an order of magnitude less than the photoelectron current, and may have resulted from higher energy photoelectrons that were emitted at small angles to the surface and bent back to the spacecraft even though they would otherwise have had sufficient energy to escape. It is also possible that the median energy gas is a low energy constituent of the solar wind, but this seems less likely to us. The highest energy component can clearly be assigned to the ambient medium, and it varies a great deal during the descent.

Curve B was recorded at an altitude of 1850 km, and shows an enhanced flux at the higher energies, and what appears to be a general hardening of the spectrum. The curve is not a simple exponential but shows irregularities. As we shall see, it seems likely that these irregularities are caused by either temporal or spatial variations in the electron flux and do not imply that the actual (instantaneous) energy spectrum is distorted in this manner. This spectrum is believed to be representative of conditions near (perhaps just outside) the bow shock, whereas curves C and D were obtained at altitudes

of 438 and 187 km, probably well inside the shock. While these four curves show a monotonically increasing flux as the altitude decreases, a more accurate picture of the altitude dependence can be obtained from figure 5, which shows the collector currents at several different potentials as a function of altitude obtained from the major frame 2 data. The altitude profiles are quite noisy, but they do hint at an apparent peak in all the currents near 700 or 800 km.

The ambient electron flux, though it has short period fluctuations, increases monotonically on the average down to below a thousand km altitude. The energy spectrum also appears to harden as the altitude decreases, but because of the flux variability and the instrument rezero at 75 volts the spectral shape is not as easily obtained. We do not imply that these changes in the solar wind electrons are simply a function of altitude; they may depend even more strongly on the magnetic connection between Mars and the spacecraft. Lander I came in on the morning side of Mars, and if the "garden hose" angle gives an even approximately realistic estimate of the solar wind magnetic field direction then Lander I should have moved into a region magnetically connected to the bow shock as it moved lower in altitude.

At altitudes below 2000 km the "photoelectron" saturation current increases and becomes quite variable (Fig. 5). This fact is not easily reconciled with our simple concept of the positive potential of the spacecraft which is required to keep the net current to the grounded metal surfaces equal to zero. Photoelectron emission from solar UV constitutes a much larger positive current to spacecraft than the impact of solar wind ions. Even the ambient solar wind electrons are inadequate to balance the loss of photoelectrons; thus the existence of the positive potential is required to reduce the photoelectron escape. But as the solar

wind electron flux increases at lower altitudes one might expect the vehicle potential to decrease, which it appears to do; in addition the magnitude of the photoelectron flux increases by a factor >2, which is not explained. Perhaps changes in the potential distribution with increased ambient density could be responsible, but it is not obvious that this is so. Below 350 km the photoelectron component disappears, presumably because the ambient plasma dominates the currents to the spacecraft and the potential changes sign.

It is possible to examine the structure in the electron fluxes at considerably smaller time scales than those shown in figure 5. The phase III data essentially provide the flux of electrons with energy greater than 15 ev (i.e. ambient electrons with energy > $\sim$9 ev) every 0.01 seconds. Two of these 2 second data blocks are shown in figure 6. At large altitudes the data are typically like that in figure 6a, i.e., the flux is very steady and shows only a few bits of noise. At lower altitudes, however, the electron flux shows rather large variations within two seconds, as illustrated in figure 6b, recorded at 1610 km. These phase III data have been linearly detrended and the noise power has been evaluated as a function of frequency by a maximum entropy method (MEM). In figure 7 the RMS deviation of the currents from the detrend line (in percent), called the coefficient of variation, and a smoothed curve of the mean phase III electron current have both been plotted vs. altitude. The mean electron current essentially follows the shape of the current profiles plotted in figure 5, and it shows an increase by a factor of 50, with a peak near 700 km. The coefficient of variation, σ, also increases to a maximum as the altitude decreases, but this maximum is approximately 1000 km above the mean flux maximum. In fact, the peak in σ occurs only slightly inside the dashed bow-shock line shown in figure 1. The relative

variation, after detrending, of the collector current from Fig. 6b is shown in the upper panel of Fig. 8. The scale of the abscissa has been converted from time to path length using the spacecraft velocity, but we do not mean to imply that temporal variations were in any way negligible. The coefficient of variation for this 2 second sample was about 12%. The corresponding MEM power spectrum is shown in the lower panel of Fig. 8. A more detailed examination of the spectral power within six different octaves is available from Fig. 9. The shaded band represents the approximate altitude of this previously noted peak in σ; similar but less distinct peaks can be seen in the power within the several spectral bands.

Theoretical Discussion

The theoretical analysis of the Phase III electron flux variations and their possible implications concerning the bow shock location has been impeded by the fact that the RPA was the only plasma instrument carried by the lander. To unambiguously determine the particular mode of wave propagation involved one ordinarily requires multidimensional plasma drift or magnetic field data, so that the wave polarization can be determined. Without such information it can also be difficult to determine the direction of propagation of the waves and the magnitude of the Doppler shift associated with the solar wind velocity. We have been able to make some progress in the absence of such complementary measurements, however, by using observations made near the earth's bow shock as a guide.

A rich spectrum of waves and oscillations has been observed in association with the earth's bow shock. The class of waves having frequencies in the spacecraft frame of about 0.5-1.5 Hz are of greatest interest in the present context. Such waves have been studied for more than a decade [Heppner et al. (1967), Russel et al. (1971)], and their general characteristics are by now quite well established (e.g. Hoppe et al., 1980).

There is strong evidence that the waves involved are right-hand circularly polarized (relative to $\underline{B}_o$) in the plasma rest frame, and that their true frequencies in this frame are several times the proton gyrofrequency. The waves are sometimes observed to exist in the form of relatively well-defined wave packets, and are of rather large amplitude ($\delta B/B \sim 1$). A number of theories have been proposed to explain their generation. One possibility (Tidman and Northrop, 1968) is that the waves are emitted by the shock itself, in the form of "precursor" and "wake" disturbances. Another possibility [Russel et al. (1971), Hoppe et al. (1980)] is that the waves are generated in the upstream solar wind plasma through instabilities driven by solar wind particles that have been backscattered by the shock. In either case, an association of the waves with the bow shock would be indicated.

In the absence of evidence to the contrary, it seems reasonable to hypothesize that the ~ 0.5 Hz variations in the electron flux to the Viking 1 lander are associated with waves similar to those described above, i.e. waves having right-hand circular polarization and a significant electromagnetic ($\delta\underline{B} \neq 0$) component. Our analysis will be based on this assumption. We shall also employ a crude "garden hose" approximation for the interplanetary magnetic field configuration.

It is thus suggested that the observed flux variations are associated with large-amplitude electron cyclotron (whistler) waves that propagate roughly parallel to the interplanetary magnetic field lines. For $\underline{k} // \underline{B}_o$ the linear dispersion relation is

$$\frac{k^2c^2}{\omega^2} = 1 - \frac{\omega_{pe}^2 + \omega_{pi}^2}{(\omega+\Omega_i)(\omega-\Omega_e)} \qquad (1)$$

For the purpose of rough numerical estimates we assume that the electron number density and background magnetic field strength are $n_o \simeq 1\ cm^{-3}$ and $B_o \simeq 3$ gammas respectively. Anticipating the result that $\Omega_i << \omega << \Omega_e$, one finds that (1) can be simplified to

$$\frac{k^2c^2}{\omega^2} = \frac{\omega_{pe}^2}{\omega\Omega_e} \tag{2}$$

The familiar physical interpretation of the wave motion can be simplified somewhat in this limit. Consider the right-hand circularly polarized electric field

$$\delta\underline{E} = \mathrm{Re}\ \{\underline{\varepsilon}(\hat{x}-i\hat{y})\exp[i(\omega t-kz)]\} \quad , \tag{3}$$

the z-axis being in the direction of $\underline{B}_o$ and $\underline{k}$. Since $\omega << \Omega_e$ the electron guiding centers undergo a $\delta\underline{E}\times\underline{B}_o/B_o^2$ drift, giving rise to the current density

$$\delta\underline{J}_e = (n_o e/B_o)\mathrm{Re}\ \{\underline{\varepsilon}(\hat{y}+i\hat{x})\exp[i(\omega t-kz)]\} \quad . \tag{4}$$

The ion motion, which is nonadiabatic ($\omega >> \Omega_i$), can be neglected, as can the displacement current. This electron current density is the source of the wave magnetic field

$$\delta\underline{B} = (\mu_o n_o e/B_o k)\mathrm{Re}\ \{\underline{\varepsilon}(\hat{y}+i\hat{x})\exp[i(\omega t-kz)]\} \tag{5}$$

The electric field induced by this time-varying magnetic field is

$$\delta\underline{E}^{ind} = (\mu_o n_o e\omega/B_o k^2)\mathrm{Re}\ \{\underline{\varepsilon}(\hat{x}-i\hat{y})\exp[i(\omega t-kz)]\} \tag{6}$$

which agrees with the initially assumed electric field (3) if (2) is satisfied. We shall return to this physical picture later in connection with the allowance for a finite wave amplitude and the question of observability.

To obtain the frequency and wavelength in the solar wind frame one must solve (2) simultaneously with the Doppler shift relation $\omega = \omega_o - \underline{k}\cdot\underline{V}_{SW}$,

where ω_o is the (apparent) frequency observed in the spacecraft frame and $\underline{V}_{SW}$ is the solar wind velocity (the spacecraft velocity is negligible in comparison with $\underline{V}_{SW}$). With $V_{SW} \simeq 400$ km/sec the garden hose approximation for $\underline{B}_o$ gives $\underline{k}\cdot\underline{V}_{SW} \simeq 0.54\ kV_{SW}$ for an inward propagating wave or $\underline{k}\cdot\underline{V}_{SW} \simeq -0.54\ kV_{SW}$ for an outgoing wave, on the morning side. With $\omega_o \simeq 2\pi/(2\ sec)$ we thus find $\omega \simeq 1.2\ sec^{-1}$, $k \simeq 9 \times 10^{-6}\ m^{-1}$ ($\lambda \simeq 700$ km) for an inward propagating wave, or $\omega \simeq 7.9\ sec^{-1}$, $k \simeq 2.3 \times 10^{-5}\ m^{-1}$ ($\lambda \simeq 270$ km) for an outward propagating wave. For the assumed magnetic field, $\Omega_i \simeq 0.3\ sec^{-1}$. Since the wave intensity is observed to peak over an altitude interval of some 300 km (Fig. 7), the inward propagating solution may not be physically significant. Note that the wavelength of the outward propagating wave is comparable to the width of the fluctuation intensity maximum; this is perhaps suggestive of a highly turbulent shock structure (which might explain the absence of any clear signature of the bow shock in the time-averaged data). The possibility of a quasi-parallel shock structure ($\underline{B}_o$ approximately parallel to the shock normal) at the point of encounter cannot be ruled out since, as noted previously, the planet was approached on the morning side. It is known (Greenstadt and Fredricks, 1979) that such shocks tend to involve strong magnetic field turbulence and do not exhibit a well-defined shock transition. Forslund et al. (1980) recently identified the condition for a quasi-parallel shock structure to exist as the requirement that electron whistlers can propagate outward along the shock normal.

It is important to consider the question of whether or not waves of the type considered here could produce observable variations in the electron flux at energies greater than 15 ev. For the sake of simplicity we shall continue to assume a single wave propagating exactly parallel to $\underline{B}_o$. The effect of a finite wave amplitude is rather easily considered for this

case. Let us assume that the electric and magnetic fields have exactly the same form as in the (linearized) model given above. The main shortcoming of that model was its neglect of the effect of the wave magnetic field on the electron motion; we shall now take this into account. Defining $\underline{u} = \underline{v} - \delta\underline{v}_D^{(1)}$, where $\underline{v}$ is the velocity of an electron and $\delta\underline{v}_D^{(1)} = \delta\underline{E}\times\underline{B}_o/B_o^2$ is the electron guiding center drift as calculated from linear theory, one finds that the equation of motion for an electron in the fields $\underline{E} = \delta\underline{E}$, $\underline{B} = \underline{B}_o + \delta\underline{B}$ reduces to

$$\frac{d\underline{u}}{dt} + \frac{e}{m_e}(\underline{u}\times\underline{B}) = -\frac{d}{dt}\delta\underline{v}_D^{(1)} - \frac{e}{m_e}\delta\underline{v}_D^{(1)}\times\delta\underline{B} \qquad (7)$$

The first term on the right of (7) is associated with a small (order ω/Ω_e) inertial drift correction to $\delta\underline{v}_D^{(1)}$, and can be ignored just as in the small-amplitude case. More importantly, the nonlinear term $\delta\underline{v}_D^{(1)}\times\delta\underline{B}$ vanishes identically for the assumed wave fields (see Eqs. 4 and 5). Thus the guiding center drift is exactly the same as that predicted by the linearized theory, while the simplified equation $d\underline{u}/dt + (e/m_e)\underline{u}\times\underline{B} = 0$ shows that the cyclotron motion ($\underline{u}$) of the electrons is now that appropriate to the self-consistent magnetic field $\underline{B} = \underline{B}_o + \delta\underline{B}$. The dispersion relation (2) thus remains meaningful, and the small-amplitude model given previously can be used to estimate the guiding center flux variations due to even large-amplitude waves.

We do not consider here the important question of the possible sideband (or modulational) instability of large-amplitude whistlers, which may be especially serious for waves propagating obliquely to $\underline{B}_o$ (Tam, 1969). It should perhaps be noted that in the case of oblique propagation the waves involved are not purely transverse, and thus involve electron number density

variations that might under some circumstances be observable.

Electron flux variations comparable to those detected by the RPA are not unexpected, however, even if the waves remain purely transverse. The above analysis shows that in the presence of a wave the electron guiding center distribution function $\bar{f}(\underline{x},\underline{v},t)$ is simply translated by $\delta\underline{v}_D^{(1)}$ in velocity space from its undisturbed form. $\bar{f}$ is here defined as the average of the ordinary Vlasov distribution function over an electron gyroperiod. For an electron of velocity $\underline{v}$ (where $m_e v^2/2 \sim 9$ ev, the lowest ambient energy that contributes to the phase III current if the spacecraft potential is assumed to be +6v) the corresponding change $\Delta\varepsilon$ in kinetic energy is approximately $m_e \delta\underline{v}_D^{(1)} \cdot \underline{v}$. The resulting fractional change in the Phase III RPA collector current should be roughly the same as that produced by varying the retarding potential through the range -15 v $\pm\Delta\phi$, where $\Delta\phi = \Delta\varepsilon/e$. From (2), (4) and (5) one finds $\delta v_D^{(1)} = (\delta B/B_o)\omega/k$, or, for the outward propagating solution found above and with $\delta B/B_o \sim 1$, $\delta v_D^{(1)} \sim 300$ km/sec. This leads to $2\,\Delta\phi \sim 6$ v. Taking the ambient electron temperature to be about 20 ev (Fig. 4b) this gives $\delta I/\bar{I} \sim 30\%$, which is comparable with the observed coefficients of variation (Fig. 7).

Summary and Conclusions

Electron current vs. retarding potential characteristic curves obtained at large altitudes showed three components, with different characteristic energies. The lowest energy flux, with an e-folding energy of about 3 ev, was probably due to photoelectrons emitted from the sunlit back side of the lander. Such electrons could gain access to the RPA sensor since their gyroradii would be large compared with the spacecraft dimensions, and the spacecraft is expected to have a positive potential relative to the plasma. The intermediate energy component is believed to have arisen from higher energy photoelectrons emitted at small angles to the surface; these electrons could be bent back toward the spacecraft even if their total kinetic energies were somewhat greater than the spacecraft potential. The highest energy component can be attributed to the ambient solar wind. From the break-point between the two higher energy components we estimated the spacecraft potential in the solar wind to be about +6 v.

As the spacecraft approached Mars the electron energy spectra showed a gradual hardening, and the roughly exponential variation gave way to irregular structure that was probably due to sudden temporal or spatial variations rather than an actual distortion of the instantaneous energy spectrum. The collector currents at various specific retarding potentials between -0.2 v. and -50 v. showed a systematic increase with decreasing altitude, reaching a maximum near 700 km. The 2 s. mean flux at energies greater than 15 ev showed a similar increase and low altitude peak, and no clear signature of the bow shock could be discerned from such data. The noise power in the >15 ev electron flux did, however, show an apparent peak

near 1700 km altitude, which is near the expected bow shock location. The integrated wave power in the 6 octaves between 0.5 and 32.0 Hz showed similar though less distinct peaks at about this altitude, with the largest spectral power appearing in the 0.5 - 2.0 Hz range.

Simple particle orbit theory calculations seem to indicate that these flux variations could have been due to large-amplitude electron whistlers, similar to waves observed previously in association with the earth's bow shock. The presence of such waves is especially probable if the shock were quasi-parallel, and hence highly turbulent. Given that the fluctuation intensity was found to peak at about the altitude expected for the bow shock crossing, and that no distinct signature of the shock could be found in the time-averaged data, it seems quite likely that this was in fact the case.

Acknowledgments

This work has been supported by NASA grants NGL 44-004-026, NGR 44-004-120 and NSG-7599.

References

Forslund, D. W., J. M. Kindel and E. L. Lindman, Simulation of quasi-parallel bow shock structures, abstract, EOS, 61, no. 17, 349, 1980.

Greenstadt, E. W. and R. W. Fredricks, "Shock Systems in Collisionless Space," in Space Plasma Physics: The Study of Solar System Plasmas, Vol. 2, part 2, National Academy of Sciences, Washington, D.C., 807, 1979.

Hanson, W. B., S. Sanatani, and D. R. Zuccaro, The Martian ionosphere as observed by the Viking retarding potential analyzers, J. Geophys. Res., 82, 4351, 1977.

Heppner, J. P., M. Sugiura, T. L. Skillman, B. G. Ledley and M. Campbell, OGO-A magnetic field observations, J. Geophys. Res., 72, 5417, 1967.

Hoppe, M., C. T. Russel and D. D. Sentman, Upstream ULF waves: implications of ISEE wave velocity measurements, abstract, EOS, 61, no. 17, 350, 1980.

Hundhausen, A. J., Composition and dynamics of the solar wind plasma, Rev. Geophys. Sp. Phys., 8, 729, 1970.

Russel, C. T., D. D. Childers and P. J. Coleman, Jr., OGO 5 observations of upstream waves in the interplanetary medium: discrete wave pockets, J. Geophys. Res., 76, 845, 1971.

Tam, C. K. W., Amplitude dispersion and nonlinear instability of whistlers, Phys. Fluids, 12, 914, 1969.

Tidman, D. A. and T. G. Northrop, Emission of plasma waves by the earth's bow shock, J. Geophys. Res., 73, 1543, 1968.

Tsurutani, B. T. and P. Rodriguez, Upstream particles and waves, EOS, 61, no. 32, 569, 1980.

Table 1

Major frame	Retarding grid potential	Suppressor grid potential	Electrometer sensitivity
0	Phase I: -75 V to 0 V Phase II: -1.5 V to 0 V Phase III: +15 V to 0 V	Phase I: +15 V Phase II: +15 V Phase III: -15 V	Rezeroed on Range 5
1	Same as I, II, III above	Phase I : -4 V Phase II: +15 V Phase III: -15 V	Rezeroed on Range 1
2	Same as I, II, III above	Phase I: +15 V Phase II: +15 V Phase III: -15 V	Rezeroed on Range 1
3	Same as I, II, III above	Phase I: -4 V Phase II: +15 V Phase III: -15 V	Rezeroed on Range 1

Table 1 RPA grid potentials and sensitivity at electrometer re-zero for a complete, four major frame instrument cycle.

Figure Captions

Figure 1. Trajectories of the Viking landers as a function of altitude and solar zenith angle. The bow shock and ionopause curves shown here are estimates, corresponding to the $H/r_o \simeq 0.25$ case of Spreiter et al. (1970), with an assumed ionopause altitude of 300 km at the subsolar point.

Figure 2. Geometry of the Viking RPA sensor head.

Figure 3. RPA retarding and suppressor grid potentials during alternate major frames of the instrument operation cycle.

Figure 4. Current vs. retarding potential characteristic curves recorded during Phase I, major frame 2, at four different altitudes on Lander 1. Blocks A, B, C and D correspond to the labeled points on the spacecraft trajectory of Fig. 1.

Figure 5. Collector currents at several fixed retarding potentials as a function of altitude, from major frame 2 data.

Figure 6. Relative Phase III collector currents vs. RPA word number (time) at (a) 11,500 km and (b) 1610 km altitude. The full time interval is 2 sec. in each case. The automatic range-changing electrometer was on Range 1 (maximum sensitivity) in (a) and Range 3 in (b). The currents show no systematic dependence on the (positive) retarding grid potential, and must thus have been due to electrons rather than ions.

Figure 7. Coefficients of variation (σ) and mean negative currents (smoothed curve) in the 2 sec. Phase III current samples, as a function of altitude.

Figure 8. Relative amplitude (after linear detrending) of the collector current from Fig. 6b, and the associated maximum-entropy-method power spectrum.

Figure 9. Spectral power within each of 6 different frequency bands as a function of altitude, for the Phase III electron currents.

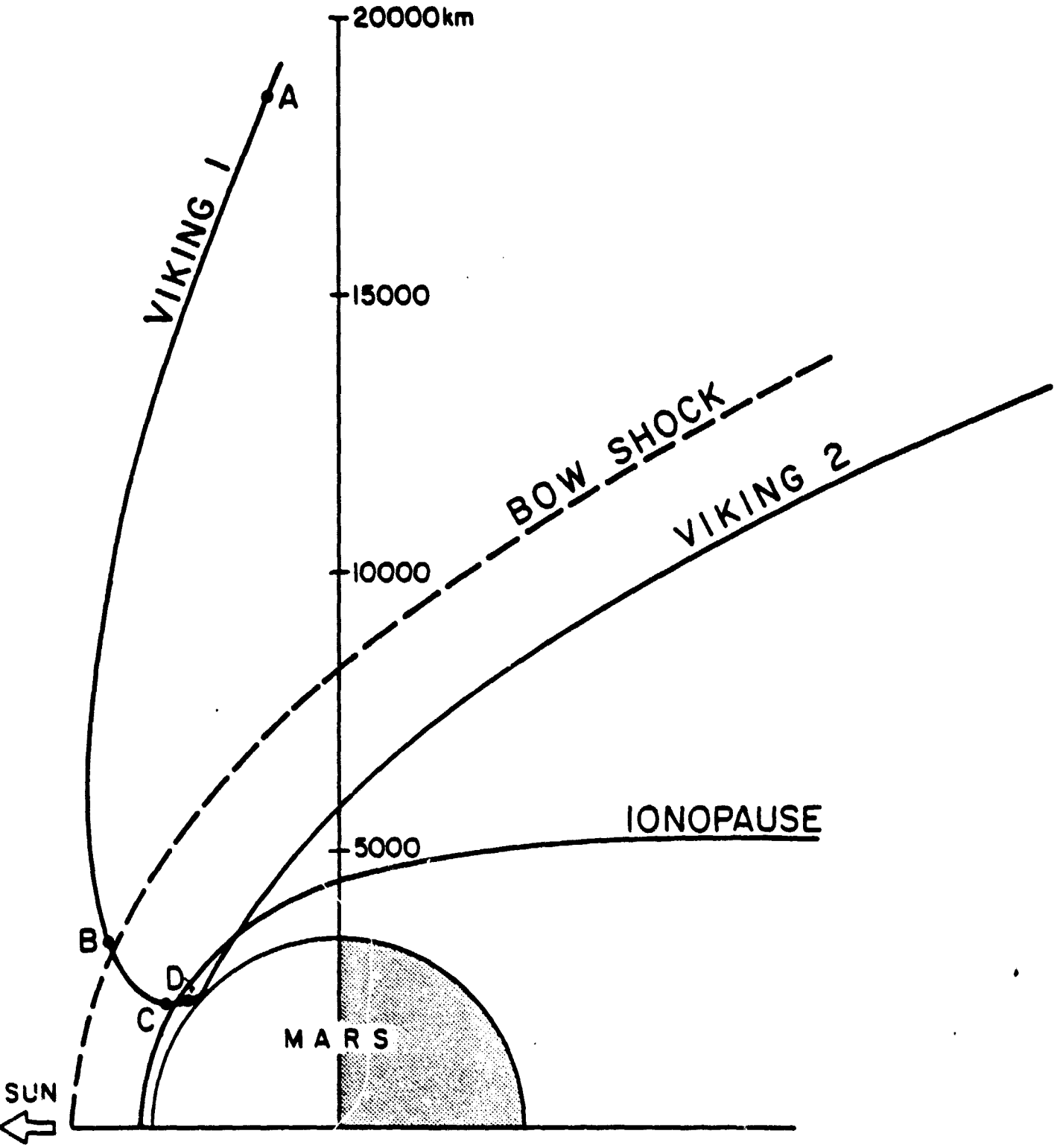
20000km
15000
10000
5000
A
VIKING 1
BOW SHOCK
VIKING 2
IONOPAUSE
B
C
D
MARS
SUN

FIGURE 1

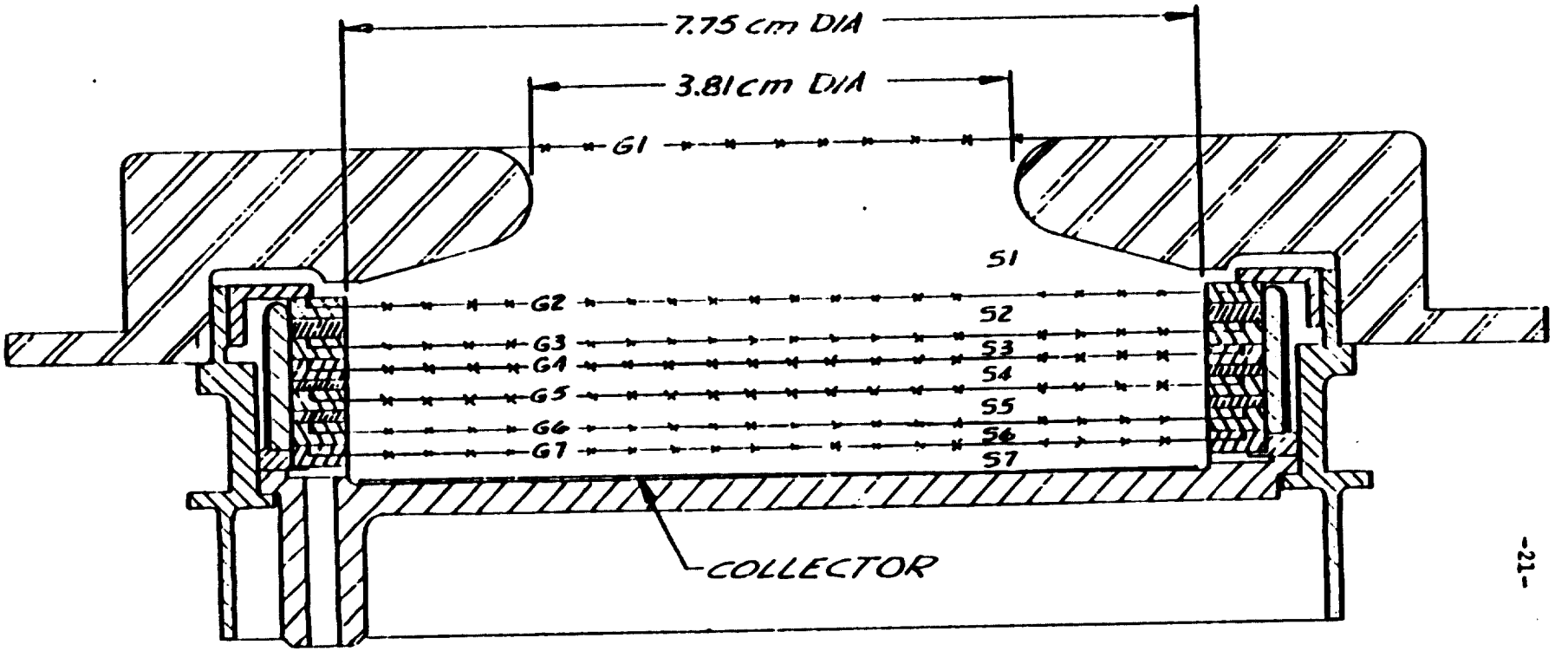

DATA CHART

GRID NO.	GRID FUNCTION	WIRES/cm	GRID SPACE	DIMENSION (cm)
G1	ENTRANCE	40	S1	1.323
G2	ENTRANCE	20	S2	.320
G3	RETARDING	40	S3	.147
G4	RETARDING	20	S4	.244
G5	SUPPRESSOR	20	S5	.244
G6	SHIELD	20	S6	.147
G7	SHIELD	20	S7	.229

VIKING RPA SENSOR

FIGURE 2

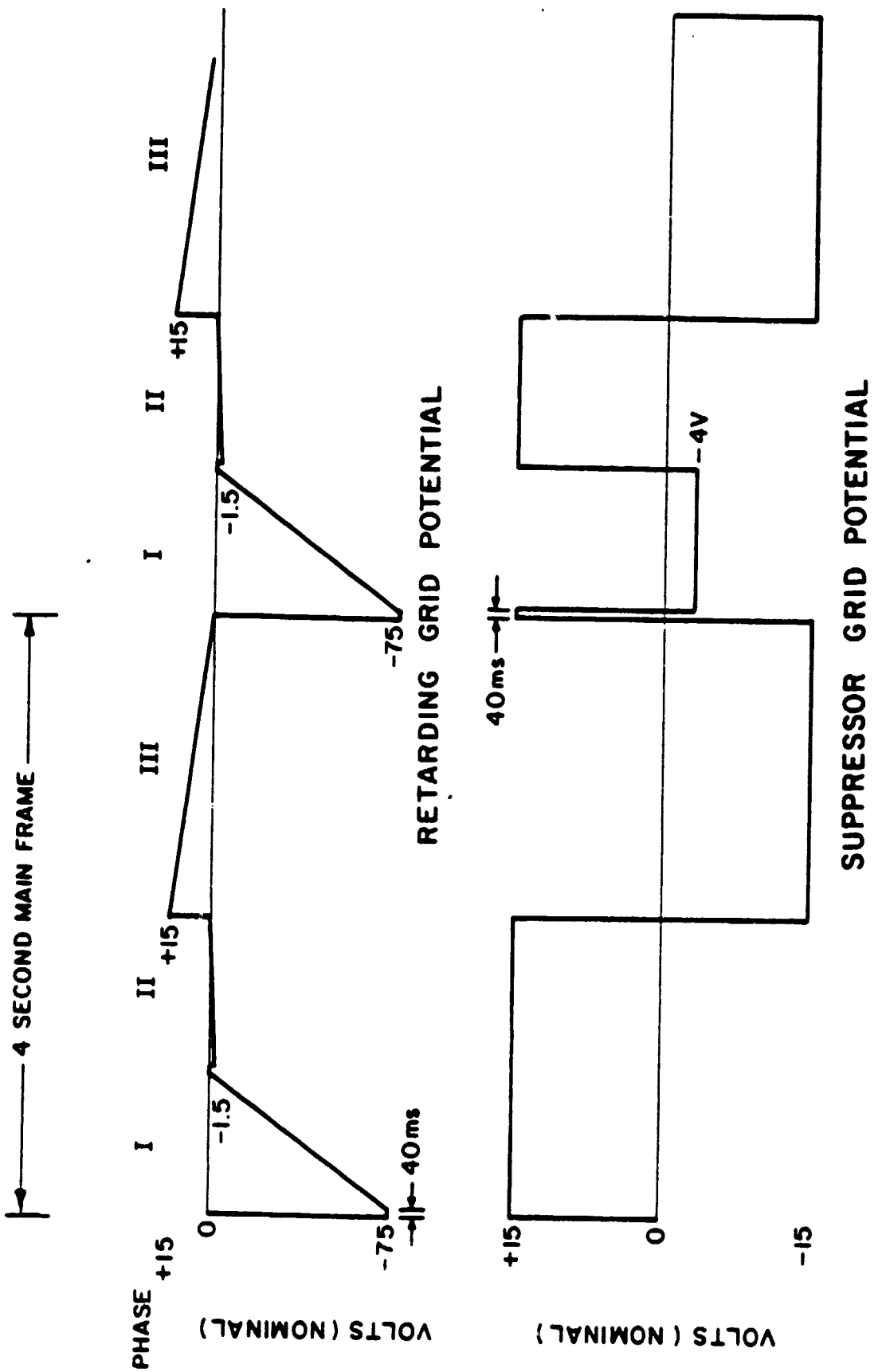
4 SECOND MAIN FRAME
PHASE
I
II
III
+15
0
-75
-1.5
40ms
VOLTS (NOMINAL)
RETARDING GRID POTENTIAL
-4V
SUPPRESSOR GRID POTENTIAL

FIGURE 3

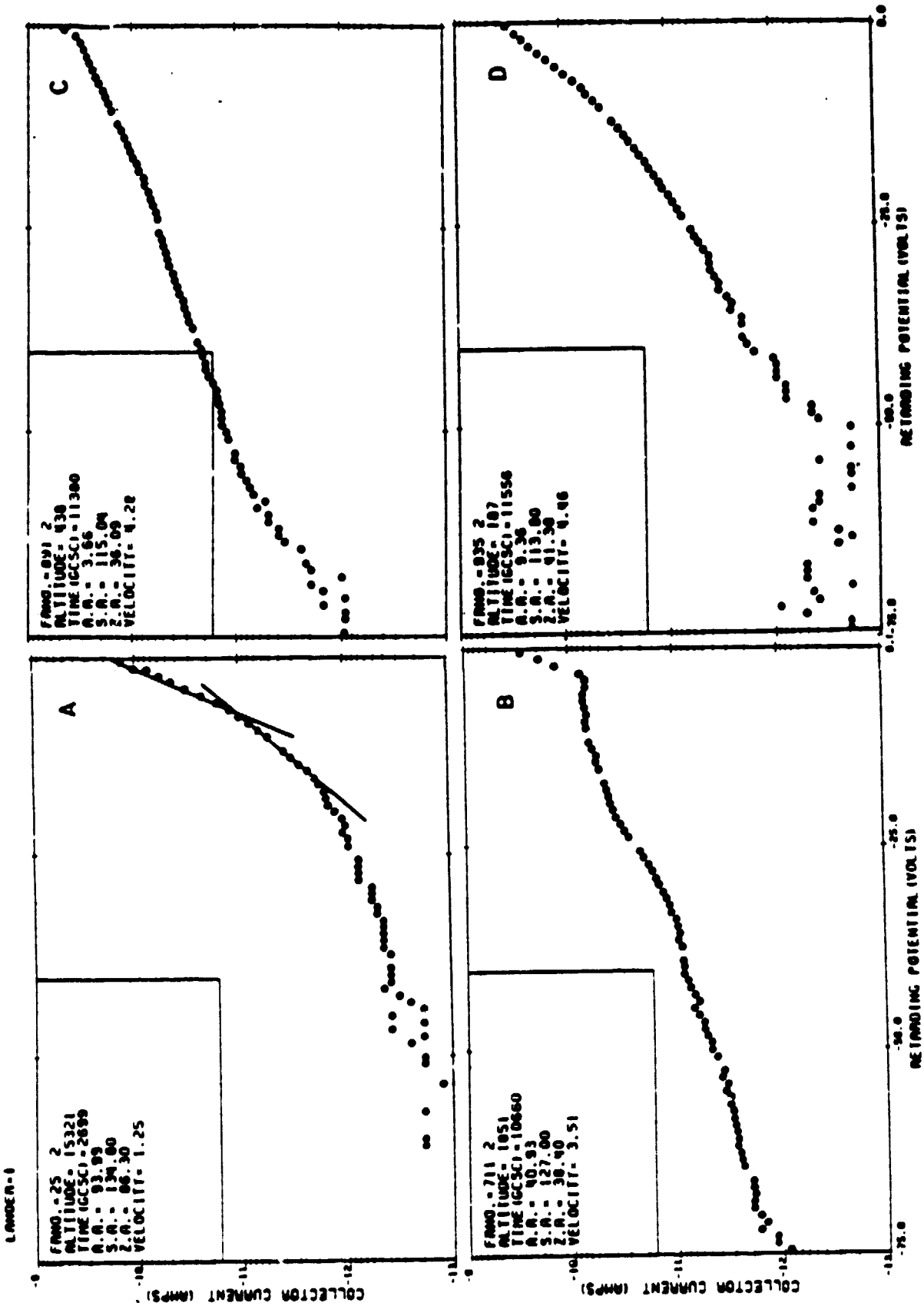
LANDEM-1
A
FRNO.-25 2
ALTITUDE- 15321
TIME(GCSC)-2899
A.A.- 93.99
S.A.- 134.80
Z.A.- 86.30
VELOCITY- 1.25
B
FRNO.-711 2
ALTITUDE- 1051
TIME(GCSC)-10660
A.A.- 90.93
S.A.- 127.00
Z.A.- 38.90
VELOCITY- 3.51
C
FRNO.-891 2
ALTITUDE- 938
TIME(GCSC)-11300
A.A.- 3.66
S.A.- 115.04
Z.A.- 36.09
VELOCITY- 4.28
D
FRNO.-935 2
ALTITUDE- 187
TIME(GCSC)-11556
A.A.- 9.36
S.A.- 113.80
Z.A.- 41.30
VELOCITY- 4.46
COLLECTOR CURRENT (AMPS)
RETARDING POTENTIAL (VOLTS)

FIGURE 4

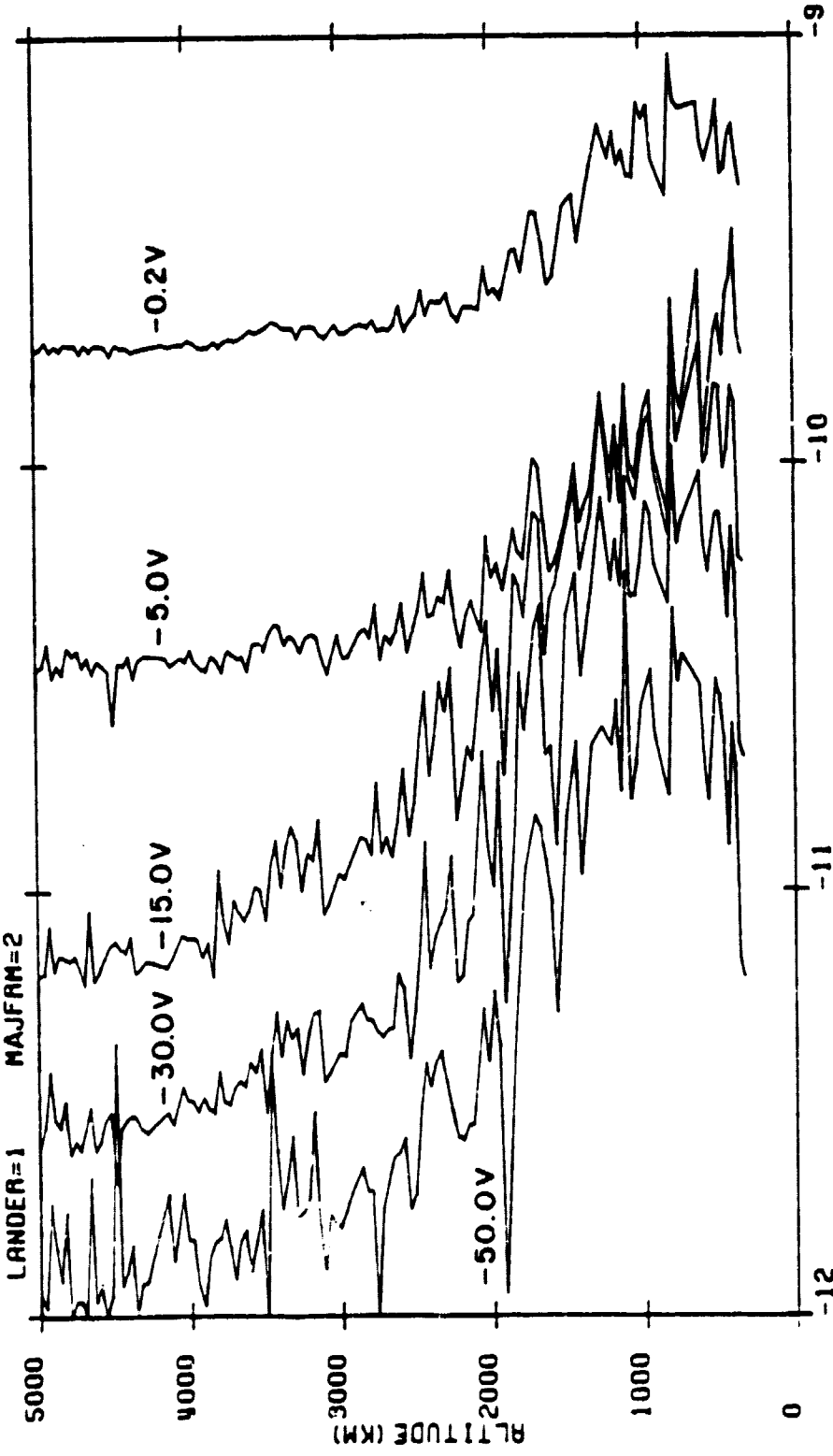
LANDER=1
MAJFRM=2
-0.2V
-5.0V
-15.0V
-30.0V
-50.0V
5000
4000
3000
2000
1000
0
ALTITUDE (KM)
-9
-10
-11
-12
LOG10 (COLLECTOR CURRENT (AMPS))

FIGURE 5

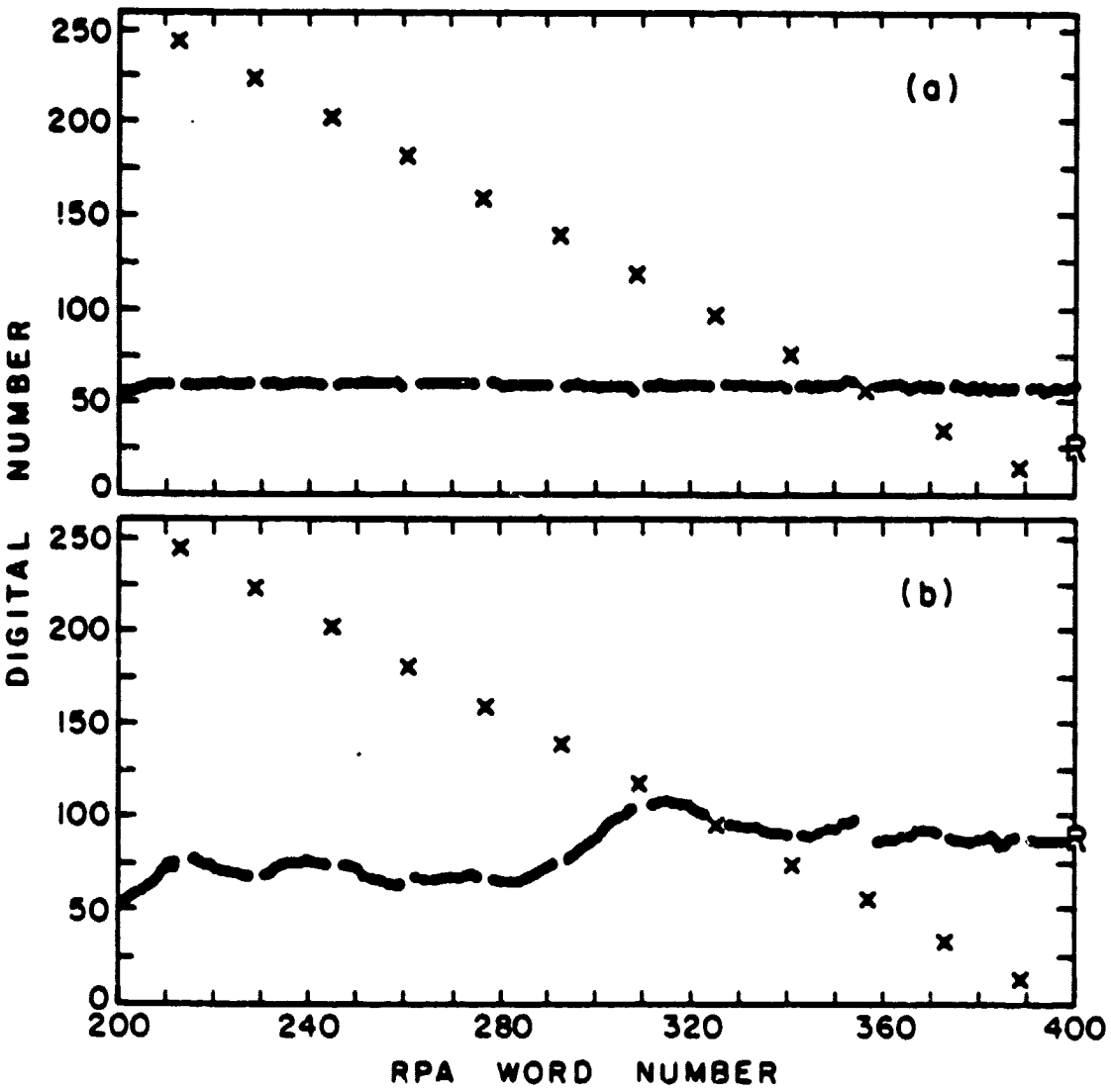
250
200
150
100
50
0
(a)
DIGITAL NUMBER
250
200
150
100
50
0
(b)
200
240
280
320
360
400
RPA WORD NUMBER

FIGURE 6

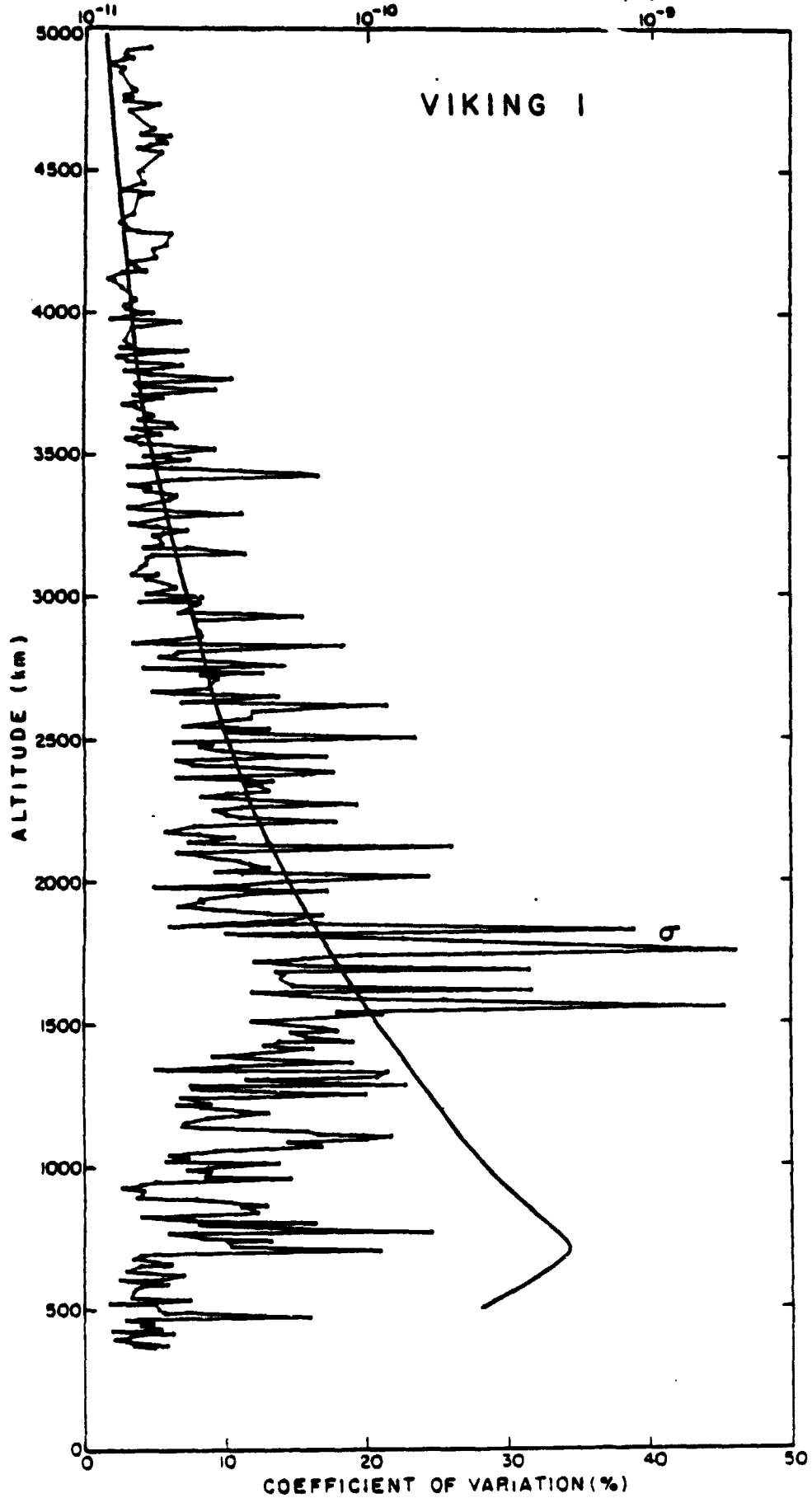

FIGURE 7

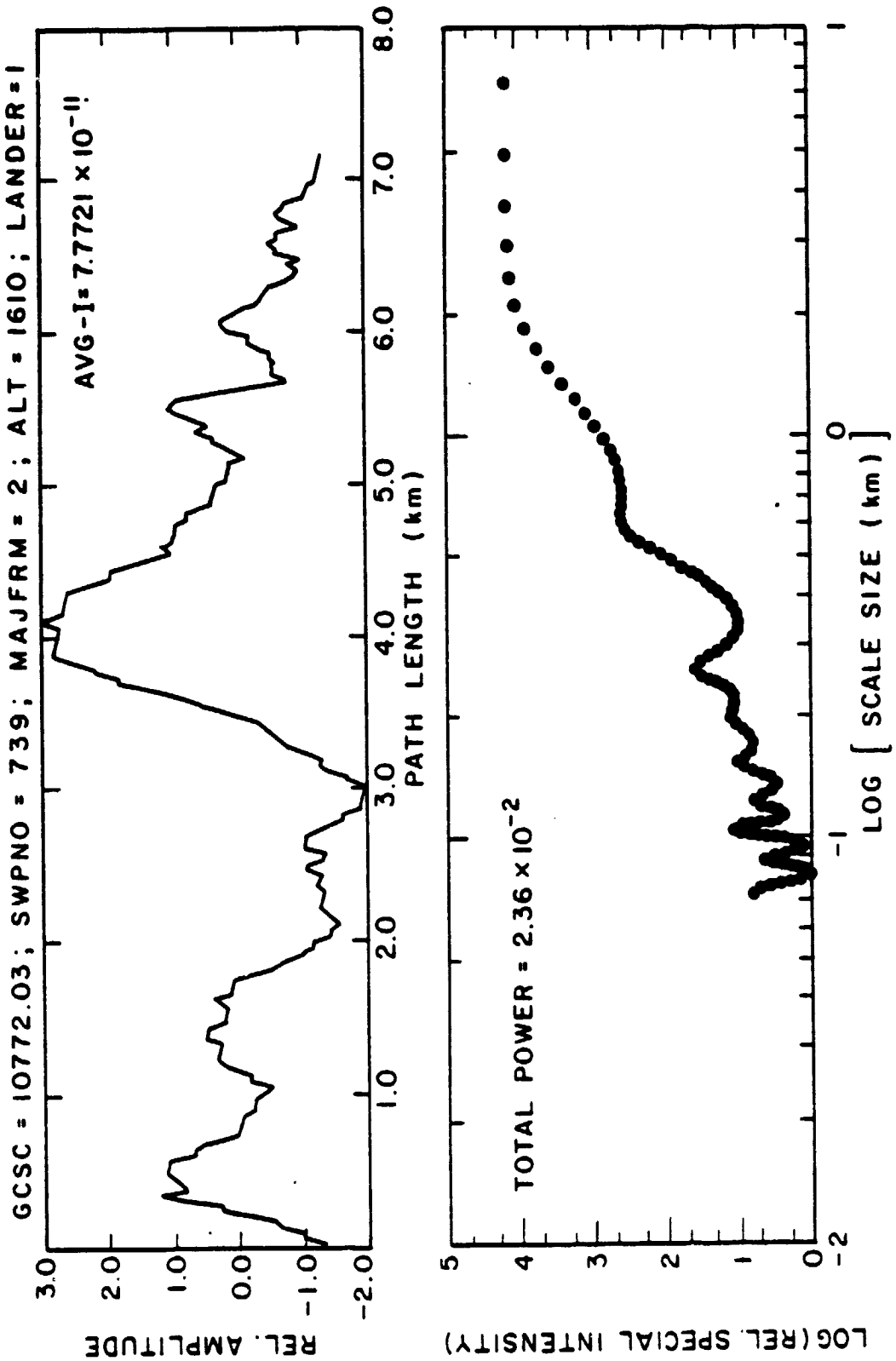
GCSC = 10772.03; SWPNO = 739; MAJFRM = 2; ALT = 1610; LANDER = 1
AVG-I = 7.7721 × 10⁻¹¹
REL. AMPLITUDE
PATH LENGTH (km)
TOTAL POWER = 2.36 × 10⁻²
LOG (REL. SPECIAL INTENSITY)
LOG [SCALE SIZE (km)]

FIGURE 8

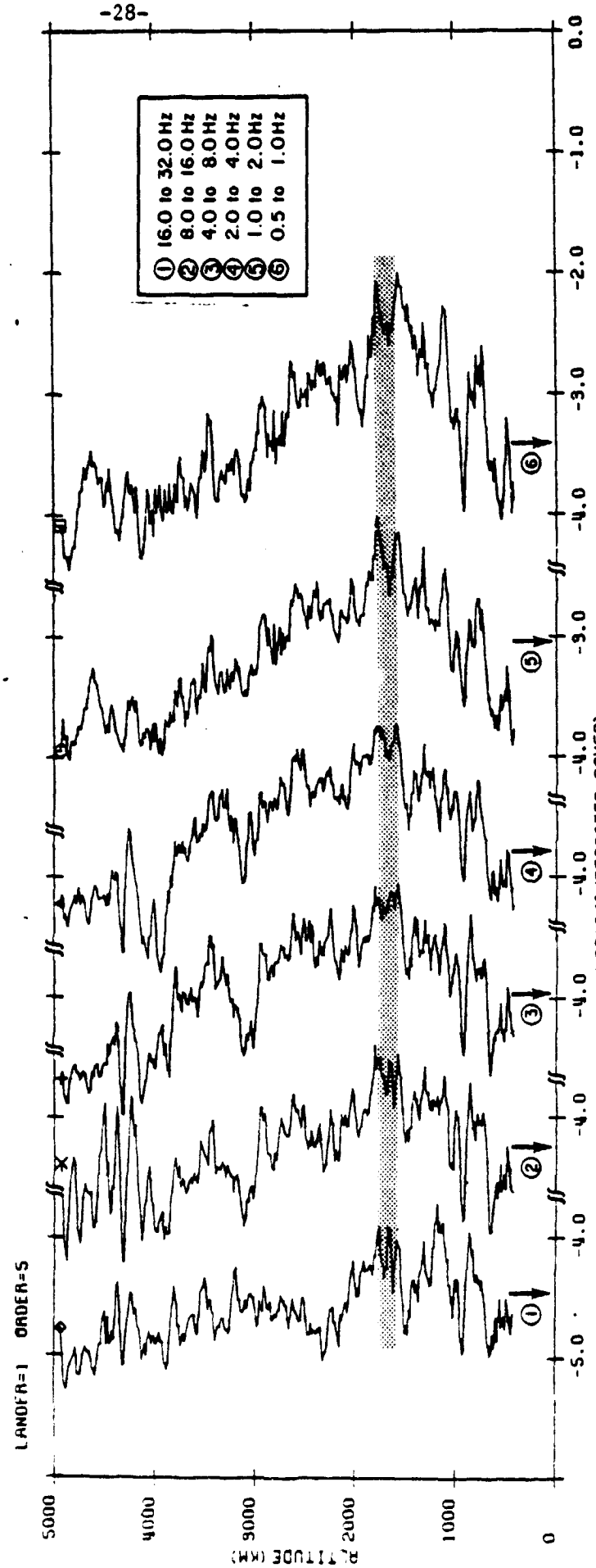
LANDFR=1 ORDER=5
① 16.0 to 32.0 Hz
② 8.0 to 16.0 Hz
③ 4.0 to 8.0 Hz
④ 2.0 to 4.0 Hz
⑤ 1.0 to 2.0 Hz
⑥ 0.5 to 1.0 Hz
ALTITUDE (KM)
5000
4000
3000
2000
1000
0
LOG10(INTEGRATED POWER)
0.0
-1.0
-2.0
-3.0
-4.0
-5.0

FIGURE 9